Evolution of oxide and nitride inclusions during processing of stainless steel

Y. Kacar[1], D. Kruger[2], and P.C. Pistorius[1]

Affiliation:
[1]Center for Iron and Steelmaking Research, Department of Materials Science and Engineering Carnegie Mellon, University, Pittsburgh, PA, U.S.A.
[2]Columbus Stainless Pty Ltd, South Africa .

Correspondence to:
C. Pistorius

Email:
pistorius@cmu.edu

Dates:
Received: 7 Oct. 2019
Revised: 23 Dec. 2020
Accepted: 21 Apr. 2021
Published: August 2021

How to cite:
Kacar, Y., Kruger, D., and Pistorius, P.C. 2021
Evolution of oxide and nitride inclusions during processing of stainless steel.
Journal of the Southern African Institute of Mining and Metallurgy, vol. 121, no. 8, pp. 379–384

DOI ID:
http://dx.doi.org/10.17159/2411-9717/923/2021

ORCID:
C. Pistorius
https://orcid.org/0000-0002-2966-1879

Synopsis

Because of its superior properties, stainless steel has been widely used for many applications. Nonmetallic inclusions can influence the quality of stainless steel products. A set of samples was used to track the response of inclusion composition during processing of a heat of titanium-bearing 18% chromium steel, from deoxidation after decarburization, to the solidified slab. The oxide inclusions responded as expected to additions of deoxidizers and calcium treatment, changing from silica to alumina and spinels, and then to calcium aluminates. The samples confirmed that titanium nitride can nucleate on liquid calcium aluminate during steel solidification.

Keywords
stainless steel, inclusion, oxides, titanium nitride precipitation, solidification.

Introduction

Nonmetallic inclusions that can be present in stainless steels include oxides, nitrides, and sulphides (Park and Kang, 2017). In this work we studied changes in oxide inclusions and the associated formation of titanium nitride and niobium carbonitride during processing of a ferritic stainless steel (containing 18% Cr). The investigation was based on a previous study that considered the change in oxide inclusions when processing a similar ferritic stainless steel in the same plant (Kruger and Garbers-Craig, 2017).

Background

The stainless steel production route typically includes melting of raw materials in an electric arc furnace (EAF), removing excess carbon by argon-oxygen decarburization (AOD) or vacuum decarburization, establishing the final temperature and composition of the liquid steel by ladle treatment, and continuous casting (Washko and Aggen, 1990). During processing, the steel can pick up nitrogen from the use of nitrogen during decarburization (in production of austenitic grades), from raw materials and exposure to the atmosphere, or nitrogen can be added intentionally. In ferritic stainless steel (based on binary Fe-Cr alloys), titanium is frequently added to bind nitrogen as titanium nitride.

In such steels, titanium nitride (TiN) normally precipitates during solidification. Titanium nitride inclusions are very hard – indeed, titanium nitride coatings extend the life of cutting tools – and such hard inclusions play an important role in microcrack formation in steel (Fairchild, Howden, and Clark, 2000). Inclusion shape is also important (*ibid.*). Because of its high entropy of melting, titanium nitride typically forms as faceted (cubic) particles with sharp corners during solidification (Fu *et al.*, 2017). The effect of angular inclusions on the mechanical behaviour of the steel can be strong: In bearing steels the deleterious effect of 6 µm TiN inclusions on the fatigue life of steel is equivalent to that of 25 µm globular oxide inclusions (Monnot, Heritier, and Cogne, 1988).

For the steel considered in this work, both titanium nitride and niobium carbonitride are expected to form during solidification: Figure 1 shows the predicted precipitation of these phases. The composition used in this calculation is that of the steel in the tundish (as measured in this work); see the sample labelled 'Tundish' in Table I (more detailed sample descriptions are provided in the section 'Steel samples'). The expected phases were calculated with Thermo-Calc (Andersson *et al.*, 2002) using the

Table I

Compositions of steel samples studied in this work (mass percentages); sample descriptions are provided in the 'Steel samples' section

Sample	C	Al	S	Ca	N	Ti	Nb	Mn	Si
AOD	0.013	0.003	0.0040	0.000	0.009	0.000	0.000	0.46	0.4
L1	0.016	0.095	0.0030	0.000	0.011	0.000	0.377	0.45	0.37
L3	0.015	0.048	0.0010	0.003	0.015	0.207	0.308	0.45	0.49
Tundish	0.015	0.034	0.0010	0.002	0.018	0.184	0.390	0.45	0.5
Slab	0.015	0.035	0.0010	0.002	0.017	0.159	0.412	0.45	0.5

Others: 18% Cr; balance Fe

TCFE9 database. Two conditions were considered: equilibrium, and Scheil-type solidification (with full mixing in the liquid, and no diffusion in the solid phases). Under equilibrium conditions, only titanium nitride would form upon solidification (Figure 1), but under Scheil conditions (severe microsegregation), niobium carbonitride would form during the last stages of solidification. The results presented later in this paper demonstrate that niobium carbonitride did form in these steel samples.

Microsegregation of niobium and titanium during solidification is the result of both an equilibrium effect (partitioning of these elements to the remaining liquid during solidification) and a kinetic effect (limited diffusion in the solid). Strong partitioning of niobium and titanium is confirmed by the partition coefficients between liquid and ferrite, as listed in Table II (calculated with Thermo-Calc and TCFE9 for the onset of solidification of the same steel composition as in Figure 1). The partition coefficient is the equilibrium ratio of the concentration (expressed as a mass percentage) of the element in the solid to its concentration in the liquid. Values far from unity indicate strong partitioning. As the table shows, little partitioning of chromium, silicon, and manganese occurs during solidification (their partition coefficients are close to unity), but titanium and niobium partition strongly to the liquid, as do carbon, nitrogen, and sulphur. Strong partitioning enhances the formation of titanium nitride and niobium carbonitride, as studied in the work reported here.

Literature survey: titanium nitride formation in stainless steel

In previous work, it was found that magnesium spinel inclusions (chemical composition: solid solution based on $MgAl_2O_4$) are present in liquid 11% Cr stainless steel that was deoxidized with aluminium (Kruger and Garbers-Craig, 2017). Alumina (Al_2O_3) is the initial oxide inclusion product that forms upon deoxidation of the steel, but tends to transform to spinel during ladle processing. The transformation can occur by transfer of magnesium from the slag to the oxide, with a low concentration of dissolved magnesium in the steel as the reaction intermediate (Kumar and Pistorius, 2018).

If spinel forms it can nucleate titanium nitride (TiN) during solidification (Fujimura *et al.*, 2011; Park, 2011; Kruger and Garbers-Craig, 2017). The small lattice misfit between spinel and TiN is stated to promote such nucleation (Park, 2011). Precipitation of titanium nitride is promoted not only by the presence of spinel nuclei, but also by strong partitioning of titanium and nitrogen to the remaining liquid during solidification (Fu *et al.*, 2017; Capurro and Cicutti, 2018).

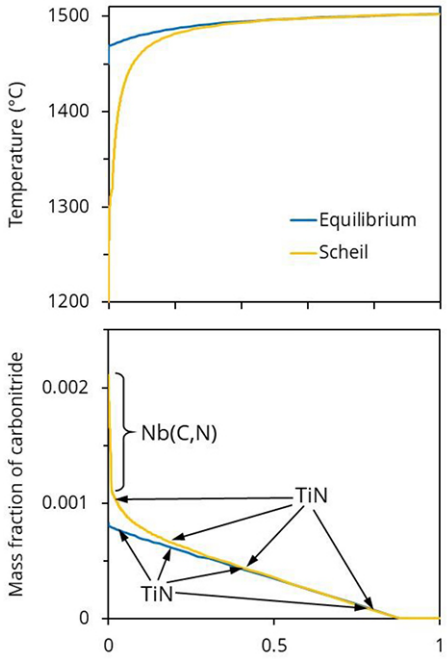

Figure 1—Calculated solidification behaviour (upper figure) and nitride and carbonitride formation (for steel with the 'tundish' composition, Table I) under equilibrium and Scheil conditions

Table II

Equilibrium partition coefficients between ferrite and liquid of elements in 18% chromium steel (at the start of solidification; liquidus temperature 1501°C; steel of 'tundish' composition in Table I). Calculated with Thermo-Calc

Cr	Si	Mn	Ti	Nb	C	N	S
1.01	0.95	0.84	0.34	0.15	0.21	0.27	0.10

Partitioning increases the concentrations of titanium and nitrogen in the last liquid that remains between ferrite dendrites.

If it forms, titanium nitride can in turn act as a nucleant for ferrite solidification in the equiaxed zone of the solidifying metal. Titanium nitride can nucleate ferrite despite the large lattice disregistry (17%) between the (111) plane of TiN and the (110) plane of ferrite: a Kurdjumov-Sachs orientation relationship between TiN and surrounding ferrite grains was found in 17% chromium steel after solidification (Fu *et al.*, 2017). The ability of TiN to nucleate ferrite is in line with the observation that the as-solidified ferrite grain size is smaller in steels with higher titanium concentrations (Park, 2011).

However, some studies showed that inclusions other than spinel can also nucleate titanium nitride. Observed nuclei included alumina (Wang *et al.*, 2013) and – in steels with negligible Al concentrations – oxides and sulphides containing magnesium (Michelic *et al.*, 2015). The ability of oxides other than spinel to nucleate titanium nitride is potentially of importance in controlling the extent and size of titanium nitride precipitation in finished steel products. To study possible nucleation by non-spinel inclusions, in this work steel samples were examined from various stages of stainless steel processing. Steel refining during these stages caused the composition of the oxide inclusions to change, from silicates (after decarburization

and deoxidation with ferrosilicon) to spinel (after deoxidation with aluminium), and finally to calcium aluminates (after calcium treatment). In addition, inclusions were examined to detect possible niobium carbonitride precipitation: titanium nitride can act as a substrate for carbonitride formation upon further solidification (Michelic *et al.*, 2015). Titanium nitride and niobium carbonitride are not expected to form while the steel is fully liquid (Figure 1), and so would not affect castability of the steel (that is, the unimpeded flow of steel through caster nozzles, unaffected by solid inclusions). However, formation of these hard phases during solidification can affect the quality of the cast product, so the distribution of these phases – and how these are affected by possible nucleation on oxides – is of great interest.

The primary aim of the work presented here was to test whether oxide inclusions with different compositions can nucleate titanium nitride during solidification. In particular, we investigated whether titanium nitride can form on liquid calcium aluminates (present after calcium treatment), in addition to the previously documented nucleation of titanium nitride by spinels (which was expected to occur in samples taken before calcium treatment).

Titanium nitride stability

Figure 1 shows that titanium nitride is expected to form during solidification. To illustrate why this phase would not form in the liquid steel at temperatures above the melting point, Figure 2 gives the calculated solubility of TiN in the steel at two temperatures: 1505°C (just above the liquidus temperature) and 1550°C. The steel composition was taken to be that of the tundish sample in this work (sample 'Tundish' in Table I), except that the nitrogen and titanium concentrations were varied. The TiN solubility was calculated with Thermo-Calc (Andersson *et al.*, 2002). For steel compositions above the solubility curve, TiN can form in the liquid by the reaction:

$$[Ti] + [N] \rightarrow < TiN > \qquad [1]$$

In this reaction, the species in square brackets are dissolved in the steel, and the angle brackets indicate the solid phase.

Figure 2 illustrates that the actual steel composition lies below the solubility curve at both 1550°C and 1505°C. Since the latter temperature is just above the liquidus temperature, these curves emphasise the prediction of Figure 1, that TiN is expected to form below the liquidus temperature after some solidification has occurred.

Experimental work

Steel samples

The process route involved melting in an electric arc furnace (EAF), decarburization followed by deoxidation in an AOD vessel, ladle treatment, and continuous casting. During the plant trial, lollipop samples of liquid steel were taken after different process steps to investigate inclusion evolution. The samples from the AOD vessel to tundish were taken from the same heat, whereas the slab sample was from a different (but similar) heat. The sequence of events is illustrated in Figure 3. As shown in Figure 3, three samples (L1, L2, and L3) were taken at different stages of ladle processing: L1 was taken after deoxidation (with Al) and addition of niobium, L2 was taken after addition of titanium, and L3 after calcium treatment. The sample labelled 'T' was taken from the tundish during subsequent continuous casting, and the slab sample was taken after solidification.

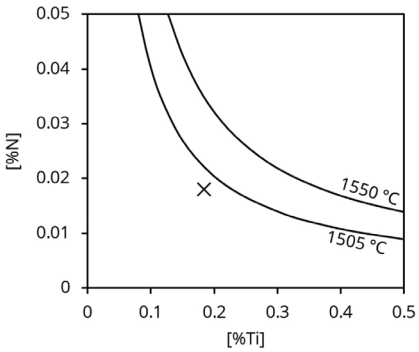

Figure 2—Calculated TiN solubility – at two temperatures – in steel with a similar composition to that studied in this work, but with variable Ti and N concentrations. The actual steel composition in the tundish is indicated by the cross

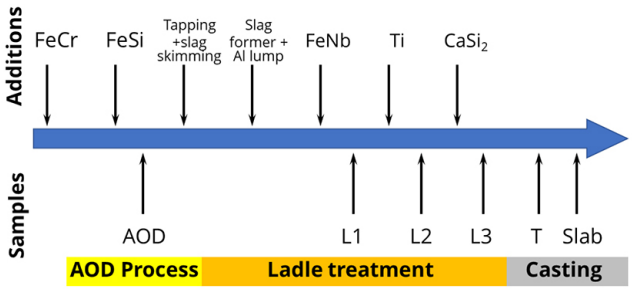

Figure 3—Sequence of events during steel production, showing additions and taking of samples. Sample descriptions are provided in the 'Steel samples' section

After decarburization in the AOD vessel, ferrosilicon was added for deoxidation and recovery of chromium from slag. The resulting silica-rich slag was skimmed off the steel before ladle treatment to prevent reoxidation and to increase alloy yield. Slag formers and aluminium lump (for deoxidation) were added subsequently. Ferroniobium was added after aluminium deoxidation; the first ladle sample was taken after this addition. Low-Al titanium scrap (98–99% Ti) was then added, and another sample taken. Some 3–4 minutes after titanium addition, calcium silicide was added for inclusion modification, and another sample taken. Five minutes of soft stirring was applied after injection of calcium silicide.

Sample analysis

Samples were polished metallographically and inclusions were analysed by automated scanning electron microscopy. Imaging and energy-dispersive X-ray (EDX) analysis were performed at an accelerating voltage of 10 kV. The instrument used a silicon drift detector with a thin window (Moxtek AP3.3). Inclusions were detected using backscattered electron imaging. Brightness levels in the backscattered electron images were standardized by setting the brightness of aluminium tape to 70 (on the dimensionless brightness scale of 0–255 used by the instrument) and that of steel to 170 (Tang, Ferreira, and Pistorius, 2017). An example of the brightness levels in a complex inclusion is shown in Figure 4. All features with brightness levels less than a set threshold of 130 were analysed. This ensured that oxide and titanium nitride inclusions were detected. EDX counts were converted to mass percentages by using the Merlet algorithm (Merlet, 1994). The minimum size of oxide and nitride inclusions

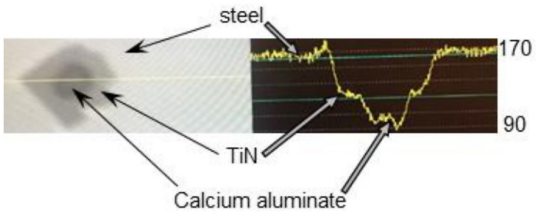

Figure 4—Example of (left) a backscattered electron (BSE) image of an inclusion (TiN around calcium aluminate) in steel, with a line scan of BSE brightness (right)

detected was approximately 1 µm. As shown later, niobium carbonitride inclusions were brighter than the steel matrix, and were evaluated by manual analysis.

Results: Inclusion changes during processing

Inclusion compositions and typical inclusion images are given in Figure 5, with average inclusion sizes (apparent size, from polished sections) and number of inclusions detected per unit area shown in Figure 6. In Figure 5, inclusion compositions are plotted as mole fractions. To show the distribution of compositions, the size of each triangular symbol is scaled proportionately to the area fraction of inclusions with a particular composition – larger triangles indicate that inclusions of that composition were more common. Although multiple elements were analysed in the inclusions in each sample, in general the inclusions contained a small set of major elements. Because quantitative analysis of oxygen and nitrogen is not reliable for micrometre-sized inclusions, the compositions are shown in terms of the metallic elements. For example, inclusions in the sample taken after deoxidation with aluminium (Figure 5b) contained mostly MgO and Al_2O_3, with CaO in a few cases; these are shown as Mg, Al, and Ca in the ternary composition plot.

Manual SEM analysis was used to confirm identification of specific inclusion types that were detected by automated inclusion analysis. For example, inclusions in the sample taken after titanium addition (Figure 5c) contained titanium nitride – which was identified from its brightness in the backscattered electron image (brighter than oxides containing Mg and Al; darker than the steel matrix), the presence of titanium, and the absence of oxygen. Similarly, niobium carbonitride (which is expected to form during the last stages of solidification of the samples; see Figure 1) was identified from its brightness (brighter than the steel matrix), presence of niobium and carbon (at higher than background levels), and absence of oxygen.

In the AOD process, oxygen diluted with argon is blown into the metal bath to decarburize the crude stainless steel. Some chromium is oxidized in the process and is taken up by the slag; ferrosilicon is added for deoxidation and chromium recovery from slag at the end of the AOD process. The resulting inclusions were mainly SiO_2, containing some traces of manganese (Figure 5a).

During subsequent ladle treatment, addition of aluminium converted the inclusions to alumina and spinel (Figure 5b). The conversion from silica to alumina occurred because aluminium has a higher affinity for oxygen than does silicon (Turkdogan, 1983). The added aluminium also deoxidized the steel more deeply, forming new oxide inclusions from the previously

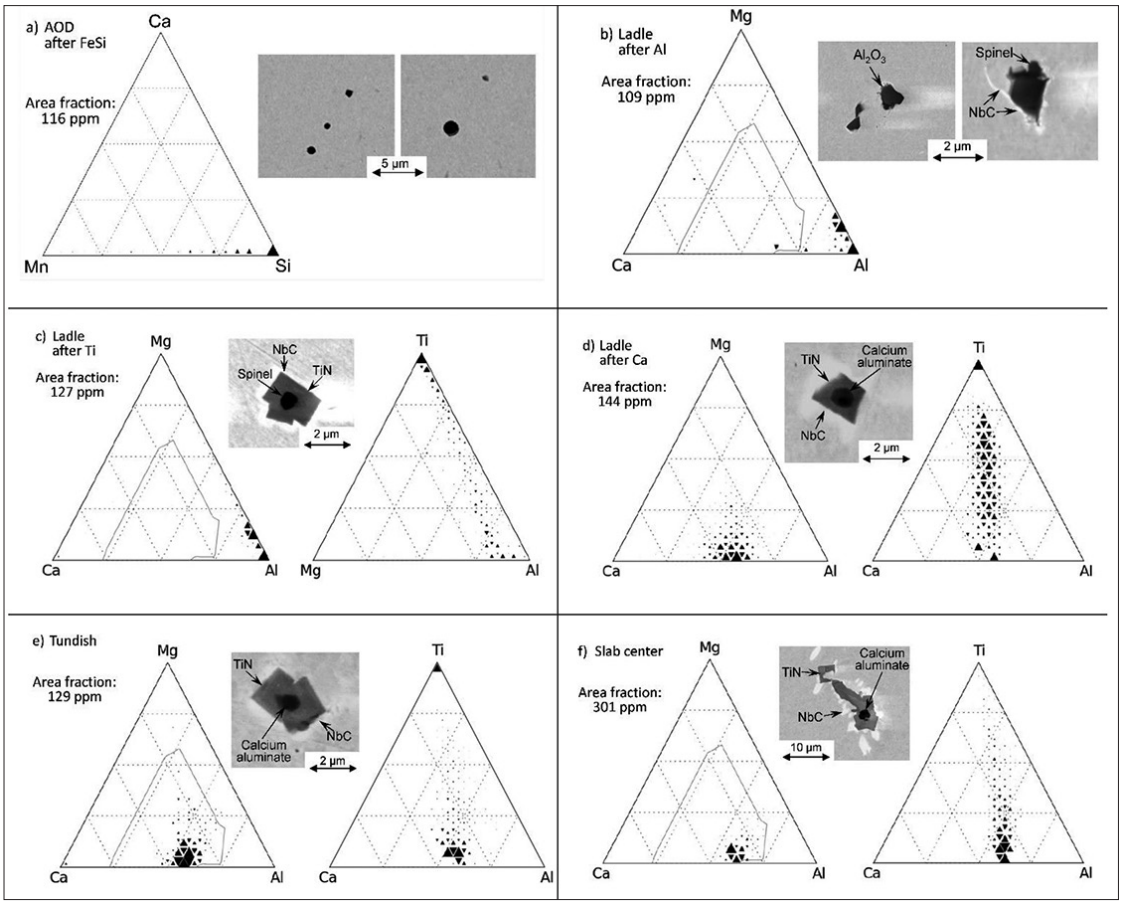

Figure 5—Distributions of inclusion compositions (in mole fractions), with examples of inclusions, for samples taken from different stages of steel processing

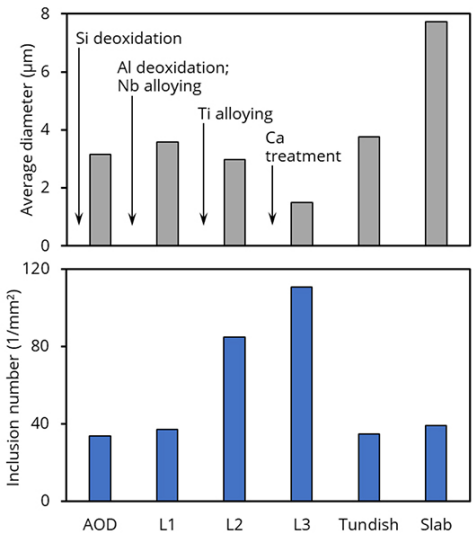

Figure 6—Changes in the average size of inclusions in samples from different stages of steel processing (upper graph), together with the number of inclusions detected (lower graph). Sample numbering corresponds to the sequence shown in Figure 3

dissolved oxygen. Although it is possible to produce stainless steels that are deoxidized with silicon only, deeper deoxidation by aluminium has several advantages:

- Ferrosilicon frequently contains some aluminium; even small aluminium concentrations can change the deoxidation product from silica to alumina and spinel (Todoroki *et al.*, 2001). Uncontrolled formation of alumina and spinel would cause clogging of caster nozzles if these oxides were left untreated. Intentional aluminium additions help to eliminate the variability in the deoxidation product caused by varying aluminium concentrations in ferrosilicon.
- If this steel grade were deoxidized with only silicon, addition of titanium would result in the formation of Ti_2O_3 or Ti_3O_5: that is, the steel would be titanium-deoxidized.

To test whether titanium oxide would form in this steel in the absence of dissolved aluminium, the equilibrium phases in steel with a composition shown in Table I were calculated, but without aluminium and with a total oxygen content of 30 ppm (by mass), for a temperature of 1550°C. The calculation was performed with FactSage 7.3 using the FSstel and FToxid databases (Bale *et al.*, 2016). The equilibrium oxide was predicted to be Ti_2O_3, with 17 ppm oxygen remaining in solution. If titanium additions were made to steel that was not deoxidised with aluminium, formation of titanium oxide would lower the titanium yield. Another side effect is that some of the resulting titanium oxide inclusions would float out in the mould during continuous casting. Titanium oxide pick-up by the mould can lead to formation of solid perovskite in the mould flux, affecting lubrication in the continuous caster mould (Mukongo, Pistorius, and Garbers-Craig, 2004).

Dissolved aluminium that remained in the steel after deoxidation further reacted with MgO in slag or refractory, transferring dissolved magnesium into the steel. The dissolved magnesium reacted with alumina inclusions to convert these to Al_2O_3-MgO inclusions (Kumar and Pistorius, 2018). MgO is only slightly soluble in Al_2O_3 (the atomic ratio of Mg to Al in Al_2O_3 at saturation is 1.1×10^{-4} at 1530°C) (Roy and Coble, 1968). Because of the near-zero solubility of MgO in Al_2O_3, any MgO pick-up caused the formation of spinel, a solid solution based on $MgAl_2O_4$. In addition to deoxidation with aluminium, the steel was alloyed with niobium before the first ladle sample was taken. Figure 5b shows that some niobium carbonitride was detected in the immediate vicinity of the alumina-spinel inclusions. Based on solidification calculations (similar to those reported in Figure 1), the niobium carbonitride precipitated during solidification of the steel sample.

Titanium alloying did not change the oxide inclusions – these remained a mixture of alumina and spinel (Figure 5c). However, titanium nitride precipitation was evident after titanium addition to the liquid steel. Figure 5c shows an example of titanium nitride precipitated on a spinel inclusion, surrounded by niobium carbonitride. This spatial relationship reflects the precipitation sequence shown by Figure 1 – during solidification, titanium nitride nucleated first (on the existing alumina and spinel inclusions), followed by niobium carbonitride formation during the last stages of solidification. The Mg-Al-Ti ternary plot in Figure 5c illustrates a continuous range of inclusion compositions, ranging from oxides (alumina and spinel) to TiN. This distribution reflects the random intersection of the sample polishing plane with inclusions containing both oxide and TiN.

Subsequent calcium treatment successfully converted the alumina and spinel inclusions to calcium aluminates containing some MgO (Figure 5d). Figure 6 shows that the size of the inclusions (oxides surrounded by titanium nitride) decreased after calcium treatment, with a corresponding increase in the number of inclusions. This has also been observed upon calcium treatment of aluminium-killed (non-stainless) steels; the decrease is caused by formation of nuclei of calcium oxide and calcium sulphide, from which the calcium aluminates grow (Ferreira, 2018). Oxide inclusion compositions that lie within the thin grey boundary in the Mg-Ca-Al diagrams would be more than 50% liquid at 1550°C – this boundary was calculated in previous work, using the MgO-CaO-Al_2O_3 phase diagram (Verma *et al.*, 2012). This is the case for the last ladle sample (as well as the tundish and slab samples), demonstrating the success of calcium treatment in converting the solid alumina and spinel inclusions to liquid calcium aluminates.

The inclusions in subsequent samples (tundish and slab, Figure 5e and 4f) are similar in composition. The inclusions consist of calcium aluminate surrounded by titanium nitride and niobium carbide. However, the inclusions in the tundish sample are somewhat larger than those in the last ladle sample, reflecting coarsening of the calcium aluminates by collision and agglomeration (Ferreira, 2018) and also some additional nitrogen pick-up (Table I). The nitrides in the slab are much larger (Figure 5f; note the difference in magnification), reflecting the much longer slab solidification time compared with the lollipop samples taken from the liquid steel.

Discussion

This set of samples confirmed that titanium nitride can nucleate on different oxide inclusions, and not just on spinels. Titanium nitride was found around spinel, alumina, and liquid calcium aluminate inclusions. Based on these results, the sizes of titanium nitride inclusions in solidified steel would depend on the number density of oxide inclusions (if fewer oxides are present, fewer titanium nitrides would form and grow larger),

the nitrogen concentration in the steel, and solidification rate. The combination of nitrogen pick-up during steel processing (Table I), reduction in the number density of oxides, and slower solidification cause the nitrides in the slab to be much coarser than in any of the samples taken from liquid steel. Macrosegregation would also affect the size and concentration of inclusions. Preliminary investigations indicated that the nitride inclusions in samples taken from near the slab surface were smaller than those from the centre of the slab, indicating a possible microsegregation effect.

Since the titanium nitrides and niobium carbonitrides formed during solidification, these would not have affected the castability of the liquid steel. Steel castability depends on the concentration and physical state of inclusions that are present in the liquid steel. From these analyses, the liquid steel contained liquid calcium aluminates (after calcium treatment), which would have ensured good castability.

Conclusions

The additions of deoxidizers and calcium during processing of an 18% Cr ferritic stainless steel resulted in the expected change in the composition of the oxide inclusions – from silica after deoxidation with ferrosilicon to alumina and spinel after deoxidation with aluminium, and finally to calcium aluminates upon calcium treatment. However, the major phase in the inclusions in the solidified samples was titanium nitride, not oxides. Titanium nitride was found to precipitate on calcium aluminates, and not just on spinels (with subsequent growth of niobium carbidonitride on the titanium nitride). The observed inclusion morphology is consistent with the expected changes during solidification (based on Thermo-Calc predictions); only oxide inclusions were present in the liquid steel; titanium nitride formed during solidification, followed by niobium carbide during the last stages of solidification.

Nucleation of titanium nitride on oxide inclusions implies that the number density and spatial distribution of nitrides would be dictated by the number and spatial distribution of oxides during steel solidification; the volume fraction of nitrides depends on nitrogen concentration. The net result is that, in the heat studied in this work, relatively coarse nitrides were present in the slab sample.

Acknowledgements

Support of this work by the Center for Iron & Steelmaking Research at Carnegie Mellon University and by Columbus Stainless Pty Ltd is gratefully acknowledged. The authors would like to acknowledge use of the Materials Characterization Facility at Carnegie Mellon University under grant no. MCF-677785. Dirk Kruger gratefully acknowledges travel support by the School on Production of Clean Steel, hosted by the Southern African Institute of Mining and Metallurgy in 2016.

References

Andersson, J.O., Helander, T., Höglund, L., Shi, P., and Sundman, B. 2002. Thermo-Calc & DICTRA, computational tools for materials science. *Calphad*, vol. 26, no. 2. pp. 273–312.

Bale, C.W., Bélisle, E., Chartrand, P., Decterov, S.A. Eriksson, G., Gheribi, A.E. Hack, K., Jung, I.-H., Kang, Y.-B., Melançon, J.,Pelton, A.D., Petersen, S., Robelin, C., Sangster, J., Spencer, P., and VanEnde, M.-A. 2016. FactSage thermochemical software and databases, 2010–2016. *Calphad*, vol. 54. pp. 35–53.

Capurro, C., and Cicutti, C. 2018. Analysis of titanium nitrides precipitated during medium carbon steels solidification. *Journal of Materials Research and Technology*, vol. 7, no. 3. pp. 342–249.

Fairchild, D.P., Howden, D.G., and Clark, W.A.T. 2000. The mechanism of brittle fracture in a microalloyed steel: Part I. Inclusion-induced cleavage. *Metallurgical and Materials Transactions A*, vol. 31, no. 3. pp. 641–652.

Ferreira, M.E. 2018. Inclusions size distributions after calcium treatment in low carbon aluminum killed steels. PhD thesis, Carnegie Mellon University.

Fu, J., Nie, Q., Qiu, W., Liu, J. and Wu, Y. 2017. Morphology, orientation relationships and formation mechanism of TiN in Fe-17Cr steel during solidification. *Materials Characterization*, vol. 133. pp. 176–184

Fujimura, H., Tsuge, S., Komizo, Y., and Nishizawa, T. 2001. Effect of oxide composition on solidification structure of Ti added ferritic stainless steel. *Tetsu-to-Hagané*, vol. 87, no. 11. pp. 707–712.

Kumar, D. and Pistorius, P.C. 2018. Rate of MgO pickup in alumina inclusions in aluminum-killed steel. *Metallurgical and Materials Transactions B*, vol. 50. pp. 181–191.

Kruger, D. and Garbers-Craig, A.M. 2017. Characteristics and modification of non-metallic inclusions in titanium-stabilized AISI 409 ferritic stainless steel. *Metallurgical and Materials Transactions B*, vol. 48, no. 3. pp. 1514–1532.

Merlet, C. 1994. An accurate computer correction program for quantitative electron probe microanalysis. *Mikrochimica Acta,* vol. 114/115. pp. 363–376.

Michelic, S.K., Loder, D., Reip, T., Ardehali Barani, A., and Bernhard, C. 2015. Characterization of TiN, TiC and Ti(C,N) in titanium-alloyed ferritic chromium steels focusing on the significance of different particle morphologies. *Materials Characterization*, vol. 100. pp. 61–67.

Monnot, J., Heritier, B., and Cogne, J.Y. 1988. Relationship of melting practice, inclusion type, and size with fatigue resistance of bearing steels. *Effect of Steel Manufacturing Processes on the Quality of Bearing Steels*, ASTM STP 987. J.J.C. Hoo (ed.). American Society for Testing and Materials, Philadelphia, PA. pp. 149–165.

Mukongo, T., Pistorius, P.C., and Garbers-Craig, A.M. 2004. Viscosity effect of titanium pick-up by mould fluxes for stainless steel. *Ironmaking and Steelmaking*, vol. 31. pp. 135–143.

Park, J.H. 2011. Effect of inclusions on the solidification structures of ferritic stainless steel: Computational and experimental study of inclusion evolution. *Calphad*, vol. 35. pp. 455–462.

Park, J.H. and Kang, Y. 2017. Inclusions in stainless steels – a review. *Steel Research International*, vol. 87, no. 12. 1700130, 26 pp.

Roy, S.K. and Coble, R.L. 1968. Solubilities of magnesia, titania and magnesium titanate in aluminum oxide. *Journal of the American Ceramic Society*, vol. 51. pp. 1–6.

Tang, D., Ferreira, M.E., and Pistorius, P.C. 2017. Automated inclusion microanalysis in steel by computer-based scanning electron microscopy: Accelerating voltage, backscattered electron image quality, and analysis time. *Microscopy and Microanalysis*, vol. 23. pp. 1082–1090.

Todoroki, H., Mizuno, K., Noda, M., and Tohge, T. 2001. Formation mechanism of spinel type inclusion in 304 stainless steel deoxidized with ferrosilicon alloys. *Proceedings of the 2001 Steelmaking Conference*, Baltimore, MD, 25–28 March 2001. ISS-AIME, Warrendale, PA. pp. 331–341.

Turkdogan, E.T. 1983. Ladle deoxidation, desulphurisation and inclusions in steel – Part 1: fundamentals. *Archiv für das Eisenhüttenwesen*, vol. 54. pp. 1–52.

Verma, N., Pistorius, P.C., Fruehan, R.J., Potter, M.S., Oltmann, H.G., and Pretorius, E.B. 2012. Calcium modification of spinel inclusions in aluminum-killed steel: Reaction steps. *Metallurgical and Materials Transactions B*, vol. 43B. pp. 830–840.

Wang, H., Sun, L., Peng, B., and Jiang, M. 2013. Inclusions for ultra-pure ferritic stainless steels containing 21% chromium. *Journal of Iron and Steel Research, International*, vol. 20, no. 10. pp. 70–74.

Washko, S.D. and Aggen, G. 1990. Wrought stainless steels. *ASM Handbook, Volume 1: Properties and Selection: Irons, Steels, and High-Performance Alloys*. ASM International, Metals Park, OH. pp. 841–907. ◆